



LUND UNIVERSITY

---

Bachelor Thesis:  
Interferometric Characterization of  
Supersonic Gas-Jets for Laser Wakefield  
Acceleration

---

Project duration: 2 months  
Author: Jonatan Henriksson  
Supervised by: Olle Lundh and Henrik Ekerfelt

Department of physics  
Division of Atomic Physics  
January 2016



## Abstract

The Multi-Terawatt laser at the LLC (Lund Laser Centre) is used to accelerate particles using laser wakefield acceleration. Laser wakefield acceleration is a particle acceleration method that utilizes intense electric fields in plasma created by high intensity laser pulses when passing through gas. A gas nozzle is used to introduce gas in the beamline to produce the plasma needed and the supersonic gas-jets produced by this nozzle were characterized in this project. Characteristics such as density profile and stability were the main focus. The method tested to characterize the jets was interferometry using a Mach-Zehnder interferometer and then treating recorded data using a MATLAB script. The main conclusion was that this method to characterize the gas works, as it can reproduce the density profile of the gas-jet, showing a density of  $0.23 \text{ kg/m}^3$  at maximum for a profile that is flat at the center of the jet and decreases beyond a certain radius using a gas pressure of 5 bar in the gas system and at 1.5 ms after the nozzle was opened.

## Acknowledgment

I would like to thank my supervisors Olle and Henrik for their help during this project. I would also like to thank Claes-Göran Wahlström for helping me find the project and come in contact with my supervisors and in general the Atomic physics division for making it possible for me to perform this work.

# Contents

<b>1</b>	<b>Introduction</b>	<b>4</b>
1.1	Laser Wakefield Acceleration . . . . .	4
1.2	Mach-Zehnder Interferometer . . . . .	6
1.3	Two-wave interference . . . . .	7
<b>2</b>	<b>Method</b>	<b>7</b>
2.1	Simulation . . . . .	7
2.2	Experimental set-up . . . . .	8
2.3	Performing measurements . . . . .	9
2.4	Data treatment . . . . .	10
2.4.1	Recovering phase difference . . . . .	10
2.4.2	Calculating Optical path-length difference . . . . .	11
2.4.3	Obtaining refractive index as a function of radius . . . . .	12
2.4.4	Density profile . . . . .	12
2.4.5	Corrections and reducing noise . . . . .	13
<b>3</b>	<b>Results and Discussion</b>	<b>14</b>
3.1	Time dependence . . . . .	14
3.2	Density profile at 5 bar . . . . .	15
3.3	Pressure dependence . . . . .	18
3.4	Sources of Error . . . . .	18
3.4.1	Computational . . . . .	19
3.4.2	Gas-jet . . . . .	19
3.4.3	Optical components . . . . .	20
3.4.4	Background . . . . .	20
3.4.5	Angle corrections . . . . .	20
<b>4</b>	<b>Outlook and Conclusions</b>	<b>20</b>
<b>5</b>	<b>Appendix</b>	<b>22</b>
5.1	Time dependence . . . . .	22

## List of abbreviations

- LLC: Lund Laser Centre
- LWFA: Laser WakeField Acceleration
- LHC: Large Hadron Collider
- CCD: Charge-Coupled Device
- FFT: Fast Fourier Transform
- FFT2: two (2) dimensional Fast Fourier Transform
- RF: Radio Frequency

# 1 Introduction

Accelerator systems are used in many fields of science, from particle physics to medicine. Developing improved (or new) systems are necessary to continue advancing science. Systems that can achieve higher energies with precision can for example increase available energy in collisions that create rare particles, leading to an increased chance to create heavier particles or give heavy nuclei enough kinetic energy to be detected before they decay. The linear accelerators today that can produce particles with highest kinetic energy are RF-cavity (Radio Frequency) accelerators, but the limited accelerating gradient produced by the components used prevent these accelerators from being improved by means of supplied power. This means that the only way to increase energy is to increase the size of the accelerator. Therefore higher acceleration gradients are needed to create more compact acceleration systems. The goal of the LWFA (Laser WakeField Acceleration) project at LLC (Lund Laser Centre) is to create a smaller accelerator system that is capable of accelerating particles by using laser wakefield acceleration.

Laser wakefield acceleration utilizes the plasma waves created when focusing a strong laser pulse into a gas that can be ionized by the lasers intensity. The electrons freed are pushed away by the ponderomotive force of the laser pulse, but the ions are much heavier than the electrons, so they can be considered stationary in comparison to the rest of the system. This creates a separation between the ions and the electrons, which results in strong fields with acceleration gradients up to 100 GV/m, while the acceleration gradient of the linear accelerators at LHC is 100 MV/m for comparison [1]. The higher acceleration gradient of LWFA leads to more optional acceleration methods, with LWFA as high energy injectors. Electrons can be trapped in these fields and accelerated to high energies under a short period of time and for a short distance [1-3].

The goal of this project was to characterize the supersonic gas-jets used in the LWFA project using interferometry. The characteristics to determine were density profile, time dependence and pressure dependence.

## 1.1 Laser Wakefield Acceleration

LWFA is a compact and relatively fast method of accelerating particles compared to RF-cavity accelerators. It is based on the production of plasma by means of high intensity laser pulses that are focused into a gas.

When a high intensity laser pulse enters a gas medium and has enough intensity to completely ionize the gas, plasma is produced as the electrons are freed from the atoms potential. Typically helium or hydrogen are used. Due to the high intensity of the pulses the ponderomotive force will force the electrons further away from the nuclei. The ponderomotive force  $\mathbf{F}_p$  is described as following:

$$\mathbf{F}_p = -\frac{e^2}{4m\omega^2}\nabla(E^2) \quad (1.1)$$

where  $e$  is the charge of the particle,  $m$  is the mass of the particle,  $\omega$  is the angular frequency of the field oscillation and  $\nabla(E^2)$  is the gradient of the squared electric field amplitude. Here it can be seen that the ponderomotive force depends on the charge of the particle squared and inversely to mass. The acceleration of the particle is then proportional to  $\frac{1}{m^2}$  as  $F = m \cdot a$ .

As the acceleration due to the ponderomotive force is proportional to squared charge and mass squared electrons are affected by this force much more so than nuclei. The squared charge to squared mass ratio of an electron is of the order of  $3 \cdot 10^{22} \text{ C}^2/\text{kg}^2$  compared to  $2 \cdot 10^{15} \text{ C}^2/\text{kg}^2$  for a helium nucleus. As all other variables describe the field, this ratio effectively represents the difference in magnitude of the acceleration between the components that are in the plasma. The acceleration experienced by the electrons is on the order of  $10^7$  higher than the acceleration experienced by the nucleus, which can be considered stationary in relation to the rest of the system. The wakefield is then a result of the electrons being pushed away from the nuclei after which they start oscillating around the nuclei.

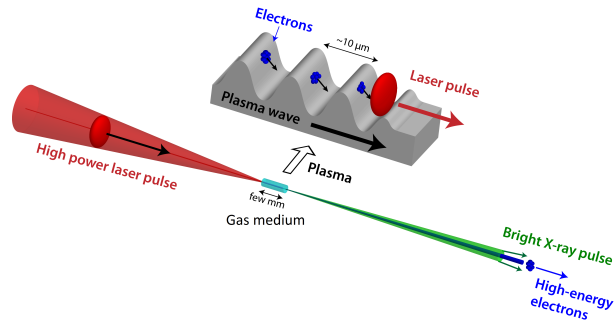


**Figure 1.1:** A representation of typical a LWFA experiment. The laser pulse is focused into a gas medium, which is as a result fully ionized and becomes plasma. The electrons are then pushed away from the nuclei due to the ponderomotive force. The separation between the ions and electrons in the plasma wakefield then produces a strong electric potential represented in the top of the figure. Injected electrons can be trapped in this potential and as the potential moves with the laser pulse they are accelerated. Figure courtesy Olle Lundh.

In Figure 1.1 the potential created in the plasma is described, showing how the wakefield oscillates, producing several potential traps where electrons can be trapped. The strength of the potential is proportional to the amount of charged particles that produce it. This relates the acceleration gradient to the density of the gas that the laser pulse passes through. As the atoms in the gas are turned into plasma, more ionized atoms result in stronger fields.

The gas can be introduced to the system using different methods. Examples of methods are gas cells [2] and supersonic gas-jets [3]. The gas cell method uses a small cell where the plasma is produced. The supersonic gas-jet method uses a gas nozzle that shoots a gas-jet into the beam. As the gas-jet is supersonic the molecules do not dissipate at the same rate as the molecules are propelled in the same direction. This results in a more even density in the jet, as molecules in a low velocity jet would. With the increased density and pressure the surrounding air is pushed away with more force. This is preferable so that the density is even throughout the jet. This is described by the density profile of the gas medium, as the refractive index of the gas and density are related. The density also affects the amount of plasma produced, representing the amount of available atoms, and therefore the strength of the wakefield. The density profile of the gas-jet then needs to be known, both for simulation of the system and to optimize the method. Obtaining the density profile can be done by interferometry.

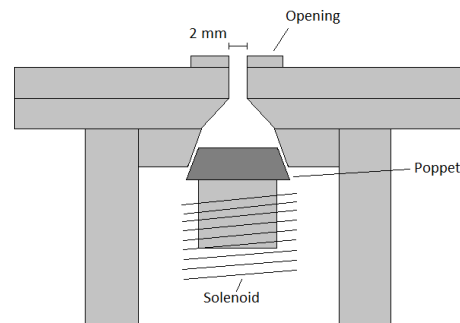


**Figure 1.2:** A schematic of the gas nozzle. It shows the valve system that is used to open and close the nozzle. The valve is constructed with a poppet that blocks gas flow, which is controlled by a solenoid magnet. The width of the cavity is gradually reduced towards the opening which accelerates the gas that is pushed through.

## 1.2 Mach-Zehnder Interferometer

There are several types of interferometers, all characterized by separating an initial wave in some manner and letting parts of the wave pass through different media, alternate paths or the same path multiple times. The different parts of the waves are then combined to create an interference pattern. Interferometers using light are most common and the Mach-Zehnder interferometer is one example of these [5].

Interferometry utilizes interference between beams of light to gain information regarding how the beams differ. For two plane, coherent and parallel wavefronts the only thing that can differ is the optical path length, resulting in an optical path difference. This is proportional to a difference in phase between the beams. If the phase difference is exactly half a period, the interference is destructive, so no light is observed. If the beams are not parallel, the interference results in a fringe pattern where the distance between the fringe maxima is proportional to one wavelength in optical path difference. A medium with different refractive index than the surrounding can be introduced into one of the beams so the interference pattern shows how the medium affected the optical path length [5].

The Mach-Zehnder interferometer used in this experiment is schematically shown in figure 1.3. The structure of the apparatus splits the incoming beam and leads them two different paths. The two beams are then recombined and if the phase has been changed, there will be interference that can be non-constructive. As one of the beams is led through a gas-jet the optical path-length is altered, due to the refractive index of the gas. This results in an interference pattern depending on distance traveled in the gas and refractive index of the gas compared to the surrounding gas [5].

The orientation of the mirrors can be used to create specific interference patterns. The angle between the two mirrors result in a controllable fringe pattern. The size and distance between the fringes depends on the angle and the wavelength of the light. The distance between the fringes is proportional to an optical path difference of one wavelength as a result of the mirrors' angle in relation to each other. An optical path difference of one wavelength means that one of the beams is delayed by one period in relation to the other beam.

An interference pattern can be used to describe how light is affected by a medium's refractive index which in turn depends on density. The two beam interference equation (see equation 1.10) can be used to show how phase difference is related to the intensity, while phase difference is also related to optical path difference which is a product of distance and refractive index. This links density to interference.

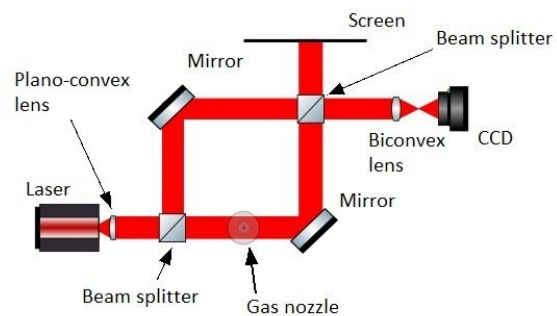


**Figure 1.3:** A schematic of the Mach-Zehnder interferometer used and all its components; two beam splitters, two plane mirrors, one biconvex lens, one plano-convex lens, a gas nozzle, a camera, a screen and a laser source. The screen was used to show the interference pattern while changing the mirror orientation.



Using lasers for interferometry is beneficial, as the light from a laser source is monochromatic, coherent and polarized. There are different types of lasers that can be used for interferometry, primarily diode lasers and gas based lasers are used [6].

### 1.3 Two-wave interference

Starting with an expression of two beams expressed by amplitude of scalar electric wavefields, one can derive the interference equation for two beams as following:

$$E_1(x, t) = A_1(x) \cdot \sin(2\pi\nu t - \phi_1(x)) \quad (1.2)$$

$$E_2(x, t) = A_2(x) \cdot \sin(2\pi\nu t - \phi_2(x)) \quad (1.3)$$

This describes the electric fields  $E_n$ , using amplitudes  $A_n$ , frequency  $\nu$ , position  $x$ , time  $t$ , and phase  $\phi_n$ . For two beams with the same frequency/wavelength there is no point in distinguishing between frequencies. The intensity is obtained by summing the two waves to express total electric field and then taking the square magnitude and time average of the total field:

$$|E_{total}(x, t)|^2 = (A_1 \cdot \sin(2\pi\nu t - \phi_1(x)) + A_2 \cdot \sin(2\pi\nu t - \phi_2(x)))^2 \quad (1.4)$$

$$= A_1^2 \sin^2(2\pi\nu t - \phi_1(x)) + A_2^2 \sin^2(2\pi\nu t - \phi_2(x)) \quad (1.5)$$

$$+ A_1 A_2 (\cos(\phi_1(x) - \phi_2(x)) - \cos(\cos(4\pi\nu t - \phi_1(x) - \phi_2(x)))) \quad (1.6)$$

$$\rightarrow \langle |E_{total}(x, t)|^2 \rangle_{time\ avg.} = \frac{A_1^2(x)}{2} + \frac{A_2^2(x)}{2} + A_1(x) A_2(x) \cos(\phi_1(x) - \phi_2(x)) \quad (1.7)$$

as the time average of  $\sin(t)$  and  $\cos(t)$  is 0 and  $\sin^2(t)$  is 0.5. The intensity  $I_{total}$  expressed in electric field amplitude is:

$$I_{total} \equiv \epsilon_0 c \langle |E_{total}(x, t)|^2 \rangle_{time\ avg.} \quad (1.8)$$

$$= \epsilon_0 c \left( \frac{A_1^2(x)}{2} + \frac{A_2^2(x)}{2} + A_1(x) A_2(x) \cos(\phi_1(x) - \phi_2(x)) \right) \quad (1.9)$$

where  $\epsilon_0$  is the vacuum permittivity and  $c$  is the speed of light, which leads to an expression containing  $I_1$  and  $I_2$  as the intensities for the two beams:

$$I_{total} = I_1(x) + I_2(x) + 2\sqrt{I_1(x) \cdot I_2(x)} \cos(\phi_1(x) - \phi_2(x)) \quad (1.10)$$

## 2 Method

The project was performed at the Multi-Terawatt laser lab at LLC (Lund Laser Centre). The project was performed in different subtasks. A simulation to understand the results of measurement was created initially, then data was recorded and treated using a script written to perform the treatment.

### 2.1 Simulation

To be able to understand the results, a simulation program was designed using MATLAB to simulate the interference pattern from a cone-shaped gas-jet. The simulation was performed by first creating two matrices, one matrix containing refractive index describing the gas-jet and one matrix containing initial intensity describing the wavefront of the laser beam. The program then iterated for each layer in the gas-jet.

The optical path length of the beam for each element was calculated depending on the refractive index in each element and the size of the element using the following equation:

$$OPL = n \cdot d \quad (2.1)$$

where  $OPL$  is the optical path length and  $d$  is distance; the equation is from [5]. The refractive index used in simulation was 1.000277 for air and 1.000036 for helium.

The phase  $\phi$  was then calculated from the optical path length, using:

$$\phi = OPL \cdot \frac{2\pi}{\lambda} \quad (2.2)$$

where  $\lambda$  is the wavelength of the light. An additional wavefront was then created with a phase calculated as if constantly passing through vacuum or air, depending on if the simulated situation is helium surrounded by air or vacuum [5].

Using the initial intensities  $I_i$  which were equal, the intensity of each element  $I_t$  was then calculated using the interference equation:

$$I_t = 2I_i \cdot (1 + \cos(\Delta\phi)) \quad (2.3)$$

Figure 2.1 shows the result of the simulation. It shows a simulated case where the wavefronts were at a vertical angle in relation to each other, which resulted in a fringe pattern seen as the horizontal lines.

The gas-jet was assumed to be circularly symmetric and having a cone-like shape with a base of 2 mm as the gas-nozzle opening was 2 mm. The figure was made to simulate the gas-jet directly above the nozzle.

The cone-like shape was assumed as the gas would most likely diverge when exiting the nozzle. The refractive index is assumed constant and have values that correspond to the gases refractive index at room temperature and atmospheric pressure. This assumed that the density of the gas was as for normal pressure and temperature. This is unlikely due to the pressurized system for releasing the gas but it describes the system. In the figure it is also shown that the displacement of the fringes is upwards, which is due to the angle between the mirrors. The angle results in non-parallel wavefronts where the phase is different depending on position in the beam. The orientation showed that since the refractive index is lower in helium the fringe displacement is in the direction towards the part of the wavefronts that have smallest distance. In the figure the wavefronts are closest at the top of the image.

## 2.2 Experimental set-up

The experimental set-up used was a Mach-Zehnder interferometer mounted on an optical breadboard. See figure 1.3 for a detailed description.

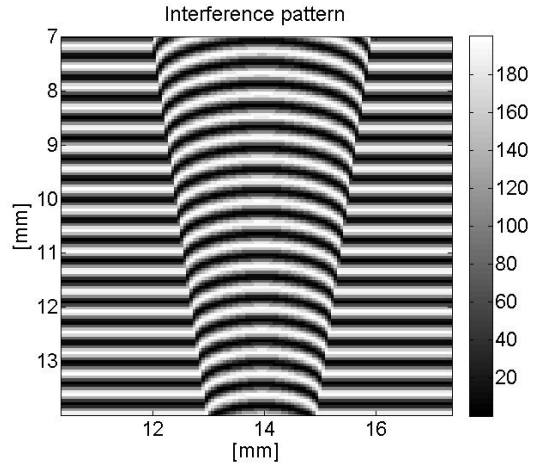


**Figure 2.1:** Simulation of interference pattern of a large angle between mirrors case using helium with air background.

The laser source was a temperature regulated single mode fiber-coupled diode laser with an output from 0 to 8 mW with a wavelength of 520 nm (green). As the source was a laser diode, the beam needed to be collimated. This was done using a plano-convex lens with a focal length of 15 cm and placing it 15 cm from the fiber cable end. The biconvex lens used had a focal length of 20 cm. To have a focused image with a size matching the chip on the CCD (charge-coupled device) camera, the size of the set-up was adjusted so the gas nozzle was placed 56 cm from the biconvex lens and the CCD was placed 31 cm from the lens resulting in a magnification of about  $\frac{5}{9}$ . All optics had a diameter of 2.54 cm.

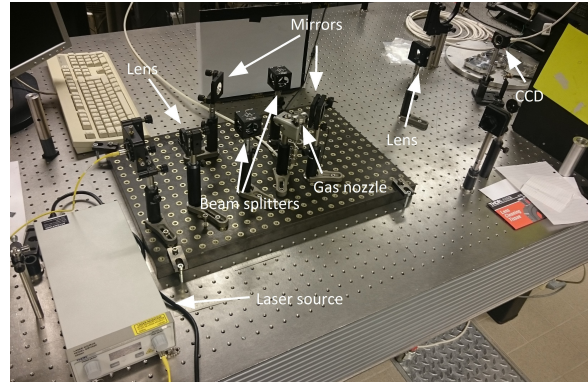


**Figure 2.2:** A picture of the actual set-up.

The CCD was connected to a computer to store the images and a trigger, that was also connected to the gas nozzle to synchronize the CCD and the gas nozzle. The trigger was capable of triggering signals with an accuracy far below milliseconds, which was the scale used for the triggering in this experiment. The scale was determined by the CCDs minimum exposure (1.5 ms). The gas system was regulated so that the pressure in the system was known.

The CCD was connected to a computer to store the images and a trigger, that was also connected to the gas nozzle to synchronize the CCD and the gas nozzle. The trigger was capable of triggering signals with an accuracy far below milliseconds, which was the scale used for the triggering in this experiment. The scale was determined by the CCDs minimum exposure (1.5 ms). The gas system was regulated so that the pressure in the system was known.

### 2.3 Performing measurements

The measurements were performed in three steps and in all steps helium was used; note that helium has lower refractive index than air.

In the first step the set-up was tested to see if it worked as planned and when to trigger the CCD in relation to when the gas nozzle was triggered so that the gas-jet had stabilized when the image was recorded. The gas nozzle was triggered to be open for 15 ms. The camera delay was used to determine that gas-jet stability was obtained 1.5 ms after the nozzle opened. The exposure for the camera was set to 1.5 ms (the shortest possible), as exposure affected saturation and error in images as result of measuring over a span of time, as apposed to a specific point in time.

The goal of the second step was to decide the optimal intensity (to avoid saturating the CCD) and magnification of the image, to check if an intensity filter was to be used and to test different orientations of the mirrors and record actual data. The power used to obtain data was 0.06 mW without filtering with an exposure of 1.5 ms.

The different orientations tested were parallel mirrors (making the wavefronts parallel) with the two beams in or out of phase, small angle between the mirrors ( $<2^\circ$ ) and a larger angle between the mirrors ( $>3^\circ$ ). The resulting images showed that the larger angle orientation resulted in less noise than having a small angle between the mirrors, while the parallel case also resulted in less noise but small inaccuracies in the angle or collimation of the beams made the background of the image uneven. The orientation of the fringes was chosen to be horizontal lines from a vertical angle difference in the mirrors as the interference due to the

gas-jet was more pronounced and less affected by the interference due to the angle between the mirrors.

In the third step more data was obtained, specifically for different pressures in the gas system and with different delays for the CCD. Different pressures and exposure delay used in this measurement can be seen in table 2.1.

**Table 2.1:** Measurement performed for pressure and time dependence. The elements containing  $\circ$  represent recorded data while elements containing  $x$  represent measurements that were not performed.

Pressure [bar] \ Time [ms]	5	6	7	8
0.5	$\circ$	$\circ$	$\circ$	$\circ$
0.7	$\circ$	$x$	$x$	$x$
1	$\circ$	$x$	$x$	$x$
1.5	$\circ$	$\circ$	$\circ$	$\circ$
3.5	$\circ$	$\circ$	$\circ$	$\circ$
5.5	$\circ$	$\circ$	$\circ$	$\circ$
10	$\circ$	$\circ$	$\circ$	$x$
14	$\circ$	$\circ$	$\circ$	$\circ$
16	$\circ$	$\circ$	$\circ$	$\circ$
18	$\circ$	$\circ$	$\circ$	$\circ$

To control if the beams were in or out of phase, the wavelength was regulated by slight changes in the current through the diode. The change in current altered the resistance and voltage over the laser diode. This changed the band gap in the pn-junction of the diode. As the band gap of a diode determines the energy of the emitted photons, the change was proportional to the change in wavelength. This was done without a detectable change in intensity. The small change in wavelength resulted in a full phase shift due to the fact that the distance the light traveled was on the scale of  $10^6$  wavelengths. Any small changes in wavelength resulted in a large but periodic change in amplitude at the intersection of the beams.

## 2.4 Data treatment

The data treatment was performed in MATLAB. The script loaded the images and converted them to two dimensional arrays where each pixel was an element with the intensity value recorded by the camera. The element values ranged from 0 to 255 in integers. The data was then treated by calculating and unwrapping phase difference from intensity. The optical path difference was calculated. Using an Abel transform optimization, a function of radius was approximated. The density profile was then obtained from the refractive index that corresponded to the optical path difference. Figure 2.3 shows an example of the recorded data.

### 2.4.1 Recovering phase difference

To recover the phase difference of each element the script was written to perform a FFT (Fast-Fourier Transform) in one dimension to check if the image had large periodic struc-

tures vertically, as this was the case for the images recorded with a fringe pattern with horizontal fringes. If there was no structure above the set threshold the data was assumed to be from a set-up with parallel mirrors.

Using the size of the nozzle in the image in pixels and the known size (6 mm) the height and width of the image were scaled to determine the actual size of the fringes. Together with the wavelength of the light this determined the angle between the mirrors.

To obtain phase difference equation 2.3 was reformulated as:

$$\Delta\phi = \cos^{-1}\left(\frac{I_t}{2I_i} - 1\right) \quad (2.4)$$

however the resulting phase difference from this equation will be periodic as arccos ranges between 0 and  $\pi$ , where the actual phase difference is cumulative. To obtain actual phase difference the resulting phase difference array needed to be unwrapped. The data was recalculated to a continuous function with MATLABs unwrapping function which corrects phase from a periodic pattern to continuous by inverting half of each period. This was done using the maximum and minimum values of intensity. Accumulation of the total phase difference was then done by adding an offset between each element depending on if the differences between an element and its neighboring elements were negative or positive.

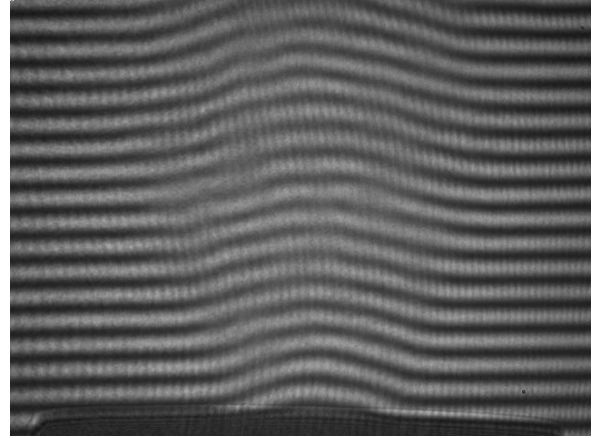


**Figure 2.3:** Recorded data for a measurement using 5 bar, larger angle between mirrors, distance decreases with height, 1.5 ms after opening nozzle and without intensity filter.

#### 2.4.2 Calculating Optical path-length difference

To obtain optical path length difference equation 2.2 was reformulated:

$$\Delta OPL = \Delta\phi \frac{\lambda}{2\pi} \quad (2.5)$$

The optical path-length difference array still contained the path-length difference due to the mirror angle for the cases where there was an angle between the mirrors. This was corrected assuming that the difference was zero at the top of the image and adding or subtracting a plane (depending on orientation) that ranged from the average value of the first row to a value in the last row for elements outside of the gas-jet. The remaining optical path difference was then due to the gas-jet. Figure 2.4 shows an example of the resulting optical path difference plot.

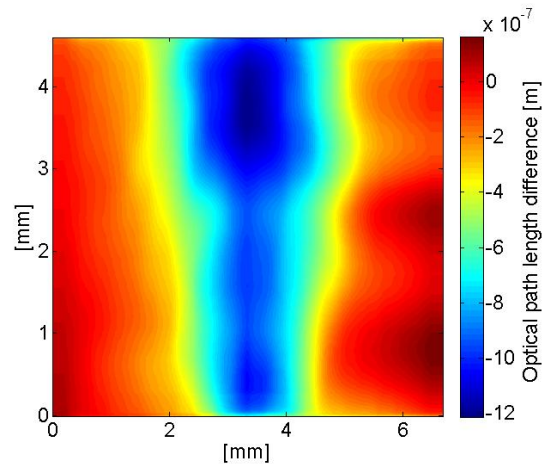


**Figure 2.4:** Calculated optical path-length difference for the case of figure 2.3.

### 2.4.3 Obtaining refractive index as a function of radius

To obtain a three dimensional refractive index profile the gas-jet needed to be described as a function of radius assuming circular symmetry at any height. To calculate the optical path-length addition per unit size (pixel) an Abel transform was used.

The Abel transform is defined as following:

$$P(x) = 2 \int_x^{\infty} \frac{F(r)rdr}{\sqrt{r^2 - x^2}} \quad (2.6)$$

where  $P(x)$  is a function of length  $x$  and  $F(r)$  is the function of radius  $r$  as seen in [7].

The way the Abel transform functions is to project a function describing propagation through a specific profile onto a plane, see figure 2.5.

The calculated array was refractive index difference, which was rescaled according to pixel size and subtracted from refractive index of air to obtain refractive index difference.

As an Abel inversion is non-trivial to implement and requires the derivative of the projected function. This would increase errors caused by background light and turbulence if a numerical differentiation was used. The Abel transform was instead used by optimizing a function of radius. The result of the transformed optimized function was compared to the polynomial fit of the optical path difference array; the polynomial fit is described in section 2.4.5. The assumed profile was an isosceles trapezoid centered at the center of the gas-jet and was optimized using three variables: height, width of top, and width of bottom. As the expected shape of the real density profile slopes are not linear, the integration would yield an error due to the shape's effect on the value of the integral. To reduce this the trapezoid was smoothed using MATLABs smooth function with a parameter optimizing the resulting curve.

### 2.4.4 Density profile

To obtain the density for each element the following equations from [9] were used:

$$\frac{(n_2 - 1)}{(n_1 - 1)} = \frac{P_2 T_1}{P_1 T_2} \rightarrow P_2 = \frac{(n_2 - 1)}{(n_1 - 1)} \cdot \frac{P_1 T_2}{T_1} \quad (2.7)$$

$$P_2 = \rho \frac{R}{M} T_2 \rightarrow \rho = \frac{P_2 M}{R T_2} \rightarrow \rho = \frac{(n_2 - 1)}{(n_1 - 1)} \cdot \frac{P_1 M}{R T_1} \quad (2.8)$$

In the first equation  $n_1$  is the refractive index of the gas at room temperature  $T_1$  and atmospheric pressure  $P_1$ ,  $n_2$  is the refractive the same gas at pressure  $P_2$  and temperature  $T_2$ . In the second equation  $\rho$  is density,  $R$  is the ideal gas constant and  $M$  is molar mass.

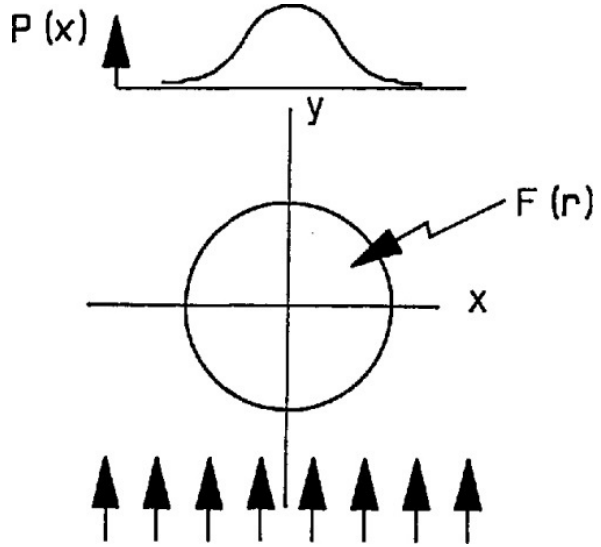


**Figure 2.5:** A description of the Abel transform.  $P(x)$  is the function of radius that is projected by the transform for a profile that has the shape described by function  $F(r)$  which can be reformulated as  $F(x, y)$ . In the shown case it is a circle, so  $r^2 = x^2 + y^2$ . For circularly symmetric systems one of the coordinates can be used to perform the transform as they behave equally in relation to the radius.[10]

The refractive index  $n_1$  was assumed helium or air depending on if the element being treated was outside or inside the gas-jet. The calculations were done under the assumption that the temperature describing the surrounding gas was room temperature and that the helium in the gas-jet behaved as an ideal gas. When plotting the density in the parts containing air the density difference is plotted instead, to make the density profile of the gas-jet clear. Since the air density is not relevant for the profile, they were set to an average value of the density difference to normal air density at atmospheric pressure and room temperature in the elements containing air.

#### 2.4.5 Corrections and reducing noise

The data treatment methods used to calculate phase difference and refractive index all increase noise and would render the results unreadable. To avoid this, three noise reduction methods were used. MATLABs FFT2 (fast-Fourier transform in two dimensions) together with a low pass circular filter was used to remove part of the noise and zero spatial frequency before unwrapping. A low pass circular filter is a two dimensional filter that removes low frequency components of a two dimensional Fourier transform. For parallel wavefront images, the noise was also reduced using MATLABs smooth function, which is an averaging filter. This was done only horizontally as to smooth the phase shift due to the gas jet which was a horizontal pattern.

The smooth function was also used to reduce noise in the optical path-length difference array, so that a polynomial function of the 5th degree could be fitted to each row of the Optical path-length array using MATLABs polyfit function. This was done to make an even profile that could be compared to the output of the Abel transform. The polynomial fit was also symmetrized around the center of the gas-jet by mirroring each half of the array. The Abel transform outputs symmetrical data and the method itself assumes circular symmetry so to compare the data to the transform it needs to be symmetrical. The Abel transform integrates the function of  $r$  from  $x$  to infinity, which is an issue when using finite numbers for numerical methods. This is solved by correcting the Optical path-length difference polynomial fit so that it goes to zero for each row towards the edges of the frame of the image, which it also should if the experimental set-up is correct and noise free as the light outside the gas-jet should be in phase after any angular corrections due to the mirrors. In doing this all values outside of the gas-jet were assumed to be noise. The correction was written to take into account that the gas-jets radius increased with height.

### 3 Results and Discussion

The following figures contain the images and treated images primarily used in developing the script and calculating results. All additional images can be seen in appendix, section 5.

#### 3.1 Time dependence

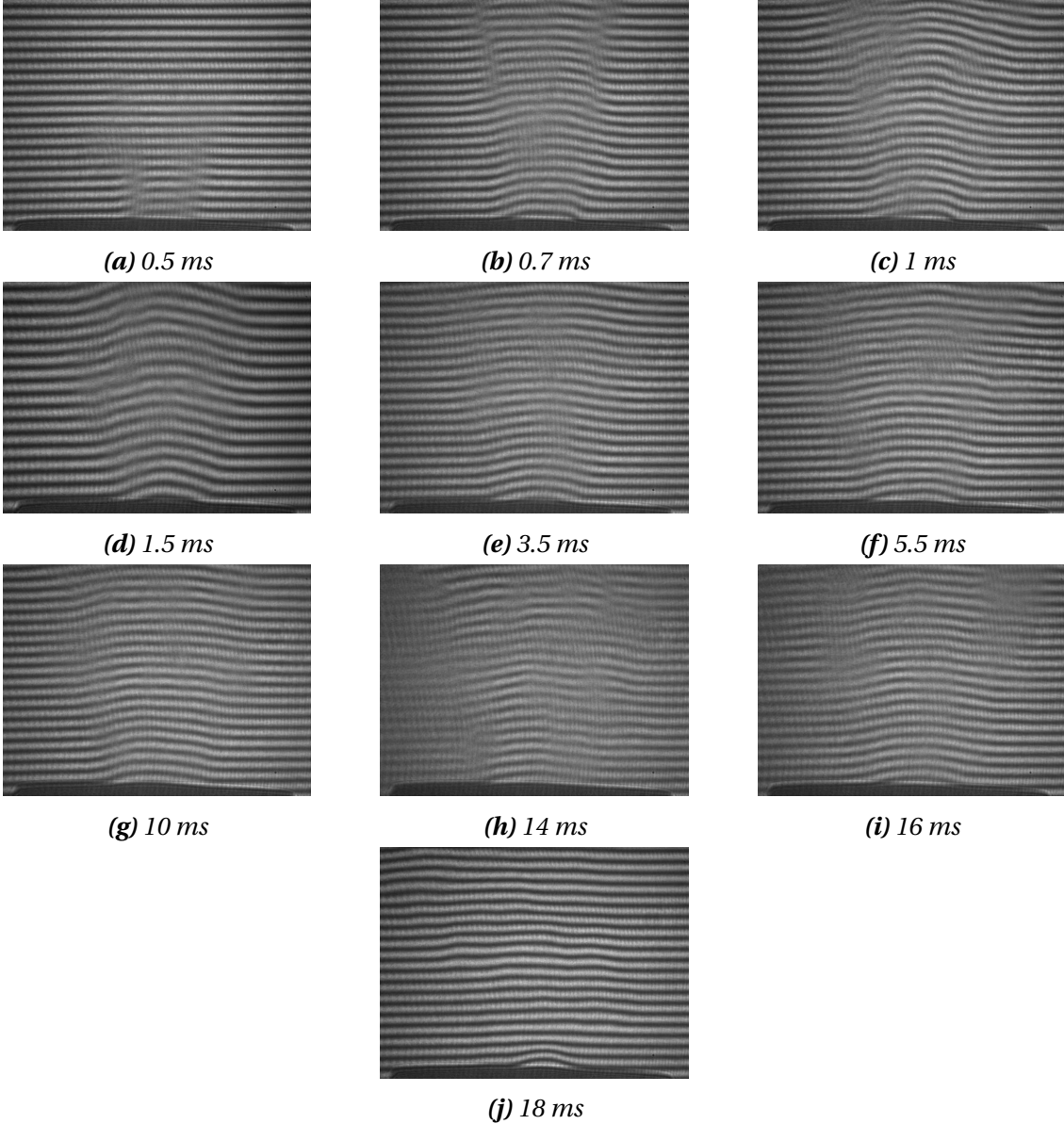


**Figure 3.1:** Images of the jet expansion at different delay with a pressure of 5 bar.

Figures 3.1a to 3.1j show the most relevant recorded data for the time dependence. They were recorded with a pressure of 5 bar in the system and for different times as can be seen the first column of table 2.1.



The stability of the gas-jet depending on time was evident without computationally treating the images, as the fringe patterns structure is a clear indicator of stability. The gas-jet was stable by 1.5 ms, as can be seen in figures 3.1a to 3.1j. As gas-jet stability was necessary for data treatment, the trigger delay for the CCD when obtaining data for treatment was chosen to be 1.5 ms. Stability is also obtained earlier than 1.5 ms with higher pressure, which is expected as the air is pushed away with more force.

Images taken 1 ms before the gas-nozzle closed show an unstable jet, possibly caused by the nozzle vibrating while shutting. As the jet is unstable at this point, laser wakefield acceleration done close to the time the nozzle closes would presumably be affected by this.

### 3.2 Density profile at 5 bar

Figures in this section show the recorded data for different methods of measurement. Also included is the result from the simulation, showing expected intensity pattern and the calculated density profiles.

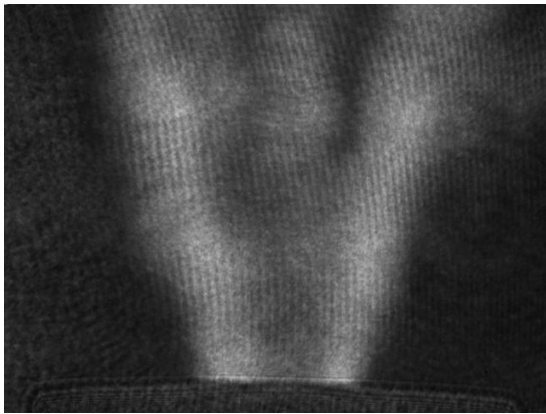


**Figure 3.2:** Measured data using 5 bar, parallel mirrors, wave-fronts out of phase, 1.5 ms after opening nozzle and with intensity filter.

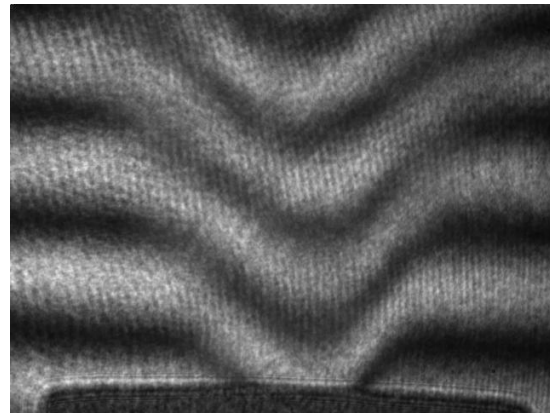


**Figure 3.3:** Measured data using 5 bar, small angle between mirrors, distance increases with height, 1.5 ms after opening nozzle and without intensity filter.

Figures 3.2 to 3.3 contain recorded images, showing the intensity pattern that resulted from the specific cases they were measured during.

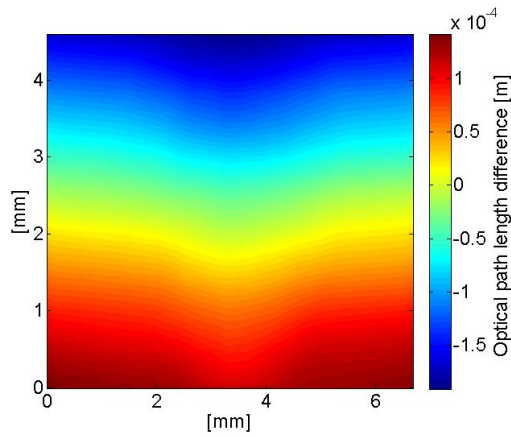


**Figure 3.4:** Calculated optical path-length difference for the same case as figure 2.4 without mirror angle correction.

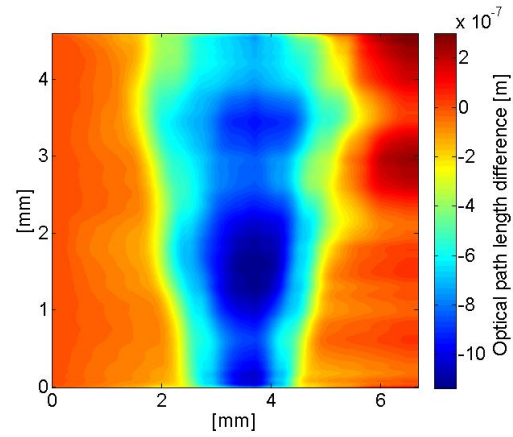


**Figure 3.5:** Calculated optical path-length difference for a case with parallel mirrors.

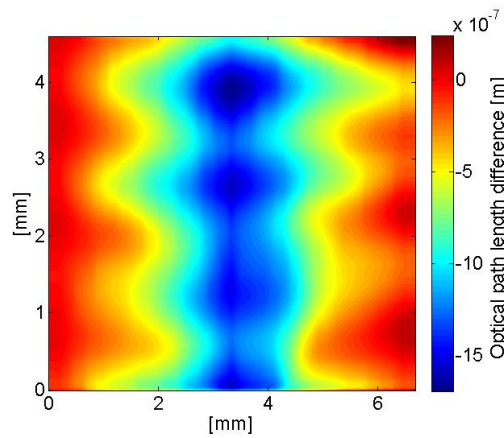


**Figure 3.6:** Calculated optical path length for small angle case. This figure shows the effects of the issue with using larger fringe patterns, as the gas jet structure is distorted in the unwrapping.

The figures above depict the calculated optical path length difference plots, showing why the large fringe pattern due to a small angle case was not used in following measurements.

Figure 3.4 shows how the wavefronts behaved and also that the mirror angle corrections were needed in the cases where the mirrors were angled. It describes the difference between the wavefronts directly. Assuming that one of the wavefronts is plane it describes how the wavefront that has passed through the helium has been affected and the orientation of the mirror.

The second figure 3.5 shows the parallel mirror case and that it could have been used in the algorithm to determine the density profile. Due to the sensitivity to errors such as turbulence or background it was not possible to replicate the images using this set-up. Thus the large angle case was chosen to be used to estimate the density profile.

Figure 3.6 shows what happened when unwrapping the small angle case data, which were distorted due to the uneven images that were recorded using this set-up.

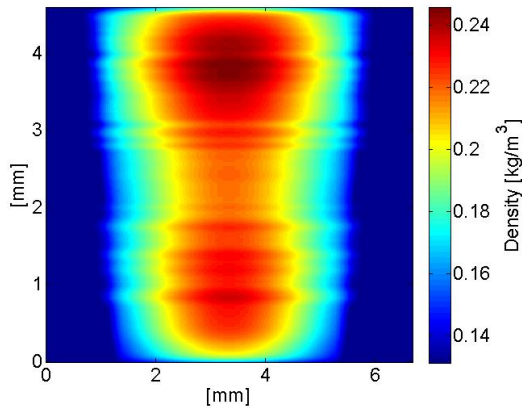


**Figure 3.7:** Density profile seen in the direction of the laser for figure 2.3.

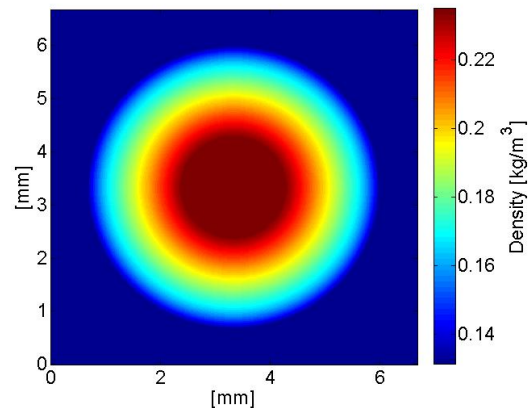


**Figure 3.8:** Simulated density profile parallel to the axis of the jet at 2 mm for figure 2.3.

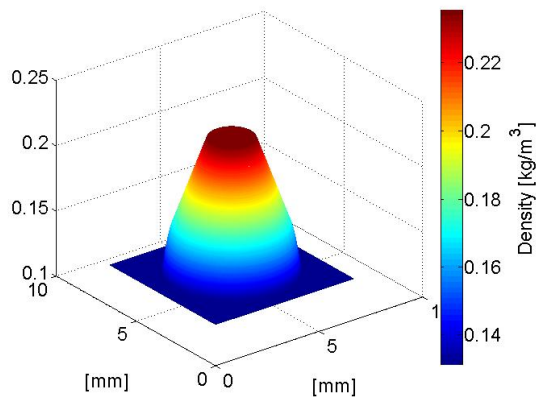


**Figure 3.9:** Plot of density profile at a height of 2 mm above the nozzle for the case in figure 2.3. Height and color represent density.

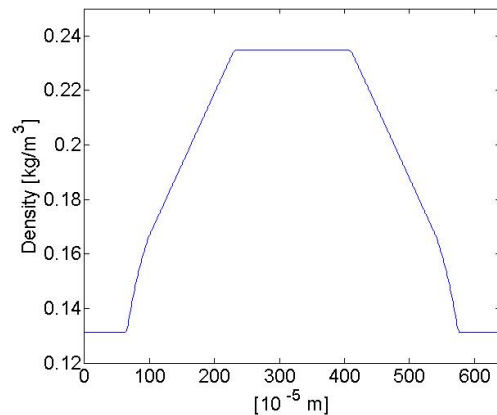


**Figure 3.10:** Plot of density profile at a height of 2 mm above the nozzle and in the middle of the jet for figure 2.3.

Figures 3.7 to 3.10 depict the resulting density profiles, shown from different directions. There is distortion in figure 3.9 that is a result of the sensitivity to noise in the Abel transform. However this effect is not visible in the other figures. The density profiles show that a few millimeters above the gas nozzle the jet has an even density, which is expected due to the gas velocity. The slopes from the center are curved due to the averaging filter. The cause of the slope shape is the size of the filter and the curve of the gas-jet profile due to gas mixing. In figure 3.7 there is a reduction of density towards the center of the jet. This is caused by the polynomial fit when fitting the polynomial to an uneven curve.

### 3.3 Pressure dependence

For all density profiles we see a similar pattern. The density increases around one millimeter from the center of the jet until it reaches a stable maximum density within a radius of one millimeter from the center for 2 mm, however the radius is different depending on height. This density depends on the pressure of the gas jet, as we see in equation 2.8. Since the higher density increases the refractive index of the gas, it approaches that of air and reduces the displacement of the fringes. If the measurements would have taken place in vacuum the displacement would presumably increase with pressure. The importance of pressure for stability can be seen in the untreated images in figures 3.11a, 3.11b and 3.11c which show less turbulence when the gas-jet is stable for higher pressures at the same time after the nozzle opened. This is expected as the higher pressure reduces the effect the air has on the jet.

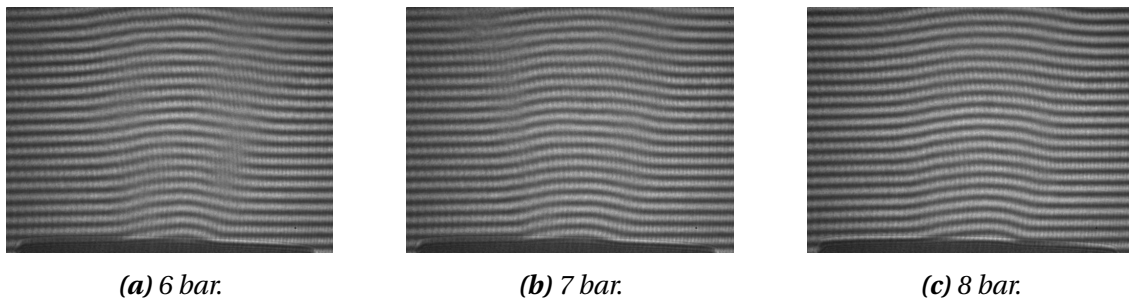


**Figure 3.11:** Images recorded at 3.5 ms delay with different pressures.

Figures 3.11a, 3.11b and 3.11c display the pressure dependence and were recorded at the same time delay after opening the nozzle (3.5 ms) at different pressures.

The characteristics of the gas-jet were extracted in different ways. To obtain details about the time dependence it was not necessary to treat the data with the MATLAB script, as the images 3.1a to 3.1j showed how the gas-jet stability and shape was changed over time. The pressure dependence required treatment by the script to be able to get values from pressure that could be used to calculate density. How the fringe pattern was affected by the pressure in the gas system could be seen from the images directly, as turbulence and displacement of the fringes are shown. For density profile it was necessary to treat the data to obtain the function of radius and a projected three dimensional profile.

### 3.4 Sources of Error

The measurements and data were affected by sources of error. These will be discussed in this section. The main sources that will be discussed are properties of the gas-jet, computational and optical. Corrections used in the algorithm such as mirror angle and background will also be discussed.

The assumptions required to perform the calculations are circular symmetry around the center of the gas-jet, equivalent beams and that gas mixing was minimal.

### 3.4.1 Computational

Circular symmetry was necessary to compare the data to the Abel transform, as Abel transform is used to calculate function of radius. To have symmetrical data the two sides of the gas-jet were mirrored and an average of the two were used for comparison with the transform.

The error if a integration method used for the Abel transform was  $h^2$  (step size squared). The error was proportional to the step size 1 and improved by the size of the interval. This error is smaller than the tolerance of the optimization, which was selected to an error of 1.25 percent. The tolerance was defined as the accepted difference between the Abel transforms output and the calculated result.

As seen in figure 3.7 the density profile at the top and bottom of the figure goes to zero, most likely due to the Fourier transform filtering. The Fourier filtering removes higher frequencies, which often consist of noise, but also distinct changes such as hard edges. This results in smoothing at the edges towards zero.

### 3.4.2 Gas-jet

The gas mixing led to an error in the slopes of the calculated density profile, as the refractive index at the mixed points increases to a value between that of helium and air. To account for this would be difficult as the refractive index change is dependent on both pressure variation and gas mixing. A possible way to account for this could be to use the Lorentz-Lorenz equation for dilute gases [8] which describes the refractive index of mixed gases. This would require estimation or measurements of the polarizability. To do the approximation the Abel transform would need to be modified so to account for an assumed gas distribution. The approximation would allow corrections to density calculation by using the Lorentz-Lorenz equations to describe the mix of gases that cause a certain refractive index in the regions close to the edge of the jet.

In figure 3.2 fluctuations are present in the top right corner of the image, seen as a slight increase in intensity outside of the gas-jet. This was most likely a manifestation of helium outside of the gas-jet caused by turbulence. In the same image inhomogeneities within the gas-jet are also present, seen as variations in intensity between left and right side of the jet. Fluctuations in the jet can also be caused by air currents but also turbulence created when the gas-jet is pushing through air. The turbulence caused local variations in density, altering pressure and therefore refractive index. Turbulence was most likely the cause of the small variations in figure 2.3. The error caused by turbulence was reduced when noise-reducing measures were taken. The larger errors due to air currents were reduced when averaging both sides after Abel transforming and during the polynomial fitting and correction.

The density in figure 2.3 shows a reduction of density from 2 mm to 3 mm above the nozzle, this is most likely due to small fluctuations in the gas-jet seen in figure 2.3, that are increased during unwrapping and the polynomial fit. This could possibly be reduced by using higher pressure data, as reducing the fluctuations which would most likely reduce this type of error exponentially.

### 3.4.3 Optical components

The optical components were a source of error, but as the variations in the components were said to be of the order of ten nm. Any variations of this kind were small to undetectable with the used equipment. The CCD camera stored integer values from 0 to 255 in arbitrary intensity units, automatically producing an error of one half for the CCD measurement interval. This resulted in a percentage error for the maximum measured value of  $\approx 0.2\%$ . To avoid saturating the CCD the intensity of the laser was set so the resulting image had maximum values slightly under 255.

The equivalency of the beams was dependent of the effectiveness of the beam splitters and the mirrors. If one mirror had less reflectance, this would have an effect on the measured intensity. This was corrected for when rescaling the phase difference to alternate around zero, as this sets any background intensity to zero.

### 3.4.4 Background

To reduce background noise the lights in the lab were off at the time data was recorded and the various corrections also reduced background noise. Any remaining background from for example reflections that were uneven and therefore not corrected for during background subtraction would have affected amplitude of the resulting density profile.

### 3.4.5 Angle corrections

The angle correction of the mirrors for the non parallel cases was performed using the number of fringes. The resulting error is then  $\pm 1$  fringe, which is proportional to a distance variation of  $\pm \lambda$  (520 nm).

## 4 Outlook and Conclusions

To summarize, the gas-jet density profile produced by the gas nozzle can be characterized using interferometry utilizing a Mach-Zehnder interferometer. The characteristics that are possible to extract using this method are density profile, stability over time and dependence on pressure, making it possible to be used for optimizing LWFA in the future. These characteristics were calculated using a MATLAB script that calculated phase from intensity, unwrapped the phase and added off-set between periods. It then calculated optical path difference and optimized a result to an Abel transform compared to the optical path difference to obtain a function of radius. The optical path difference as function of radius was then recalculated to refractive index which was used to determine pressure and then density profile. Since the computational methods were sensitive to noise the data was treated to reduce noise, which was done using Fourier transform filtering and averaging filter functions. The gas-jet characteristics are dependent on what gas is used due to density and refractive index. The pressure used in the gas system affects the stability of the jet. The jet is stable about 1.5 ms after the nozzle opens but stabilizes quicker using higher pressure. The jet becomes unstable again ca 1 ms before the nozzle closes, due to vibrations in the system when the nozzle is starting to close as the exposure for the CCD camera was 1.5 ms.

## References

- [1] **Tomás R.** Overview of the Compact Linear Collider. <http://journals.aps.org/prab/pdf/10.1103/PhysRevSTAB.13.014801>.
- [2] **Reymond S.** *Optical density measurements of a variable-length gas cell for laser wakefield acceleration* (Technical report). Lund, Department of Atomic Physics, Lund University.
- [3] **Lundh O.** *Laser-driven beams of fast ions, relativistic electrons and coherent X-ray photons*. Lund : Department of Physics, Lund University, 2008.
- [4] **Amiranoff, F. and Baton, S. and Bernard, D. and Cros, B. and Descamps, D. and Dorchies, F. and Jacquet, F. and Malka, V. and Marquès, J. R. and Matthieussent, G. and Miné, P. and Modena, A. and Mora, P. and Morillo, J. and Najmudin, Z.** Observation of Laser Wakefield Acceleration of Electrons. *Phys. Rev. Lett.*81-5: p.995-998,1998.
- [5] **Pedrotti FL, Pedrotti LM, Pedrotti LS.** *Introduction to Optics*. Harlow: Pearson Education Limited, 2014, p. 29 , 135, 174-176, 202-209.
- [6] **Saleh BEA, Teich MC.** *Fundamentals of Photonics*. New York: Wiley, 2007, p. 567-575,716.
- [7] **Goree J, Bin Liu, Drake D.** Gas flow dependence for plasma-needle disinfection of *S.mutans* bacteria. *Journal of Physics D: Applied Physics* 39: C3479–C3486, 2006.
- [8] **McConnell SR.** Gas Detection by use of Sagnac interferometer [Online]. Queensland University of Technology. [http://eprints.qut.edu.au/16701/1/Sean\\_McConnell\\_Thesis.pdf](http://eprints.qut.edu.au/16701/1/Sean_McConnell_Thesis.pdf) [30 Nov. 2015].
- [9] **Moran MJ, Shapiro HN, Boettner DD, Bailey MB** *Fundamentals of Engineering Thermodynamics*. New YorkG: Wiley, 2000.
- [10] **Dasch CJ.** One dimensional tomography: a comparison of Abel, onion-peeling, and filtered backprojection methods. *Applied Optics Vol. 31, Issue 8, pp. 1146-1152 (1992)*.

# 5 Appendix

## 5.1 Time dependence

The following images were recorded with larger angle between mirrors.

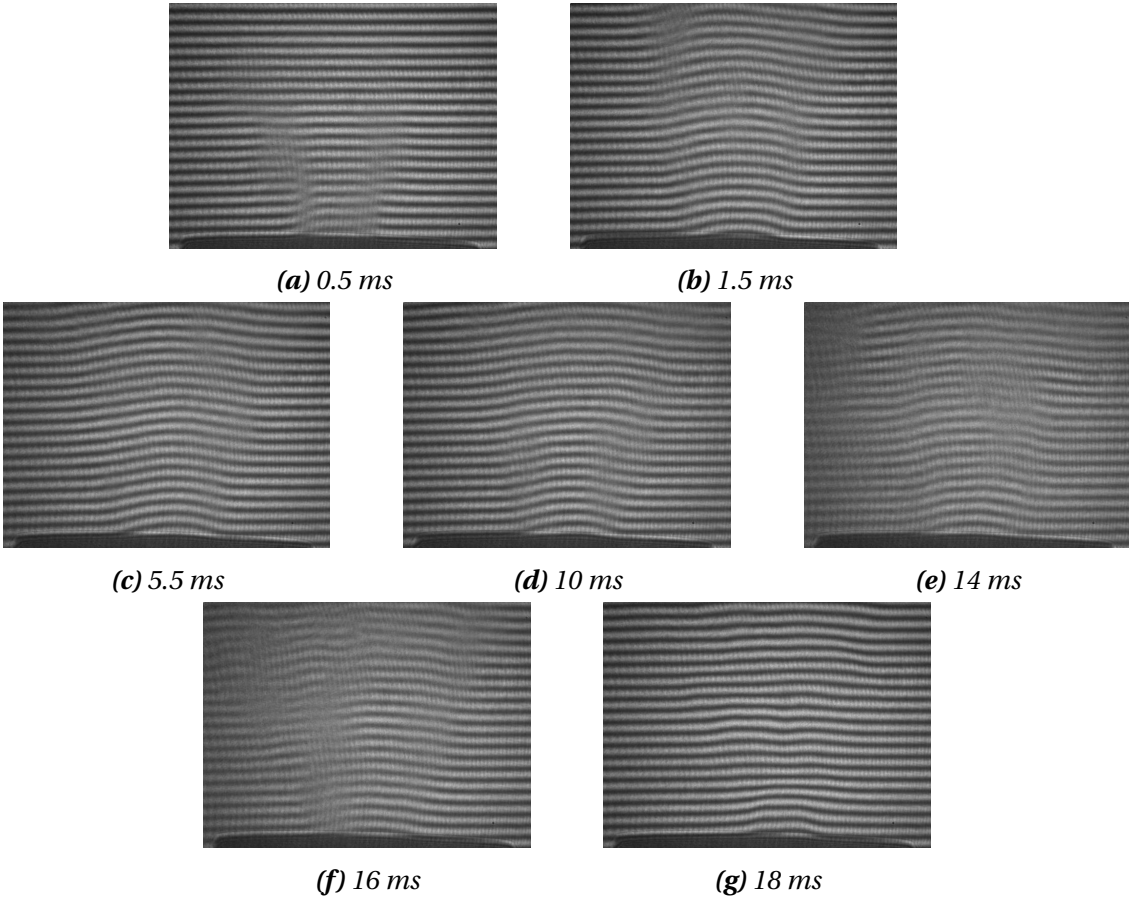


**Figure 5.1:** Images recorded at 6 bar with different exposure delay



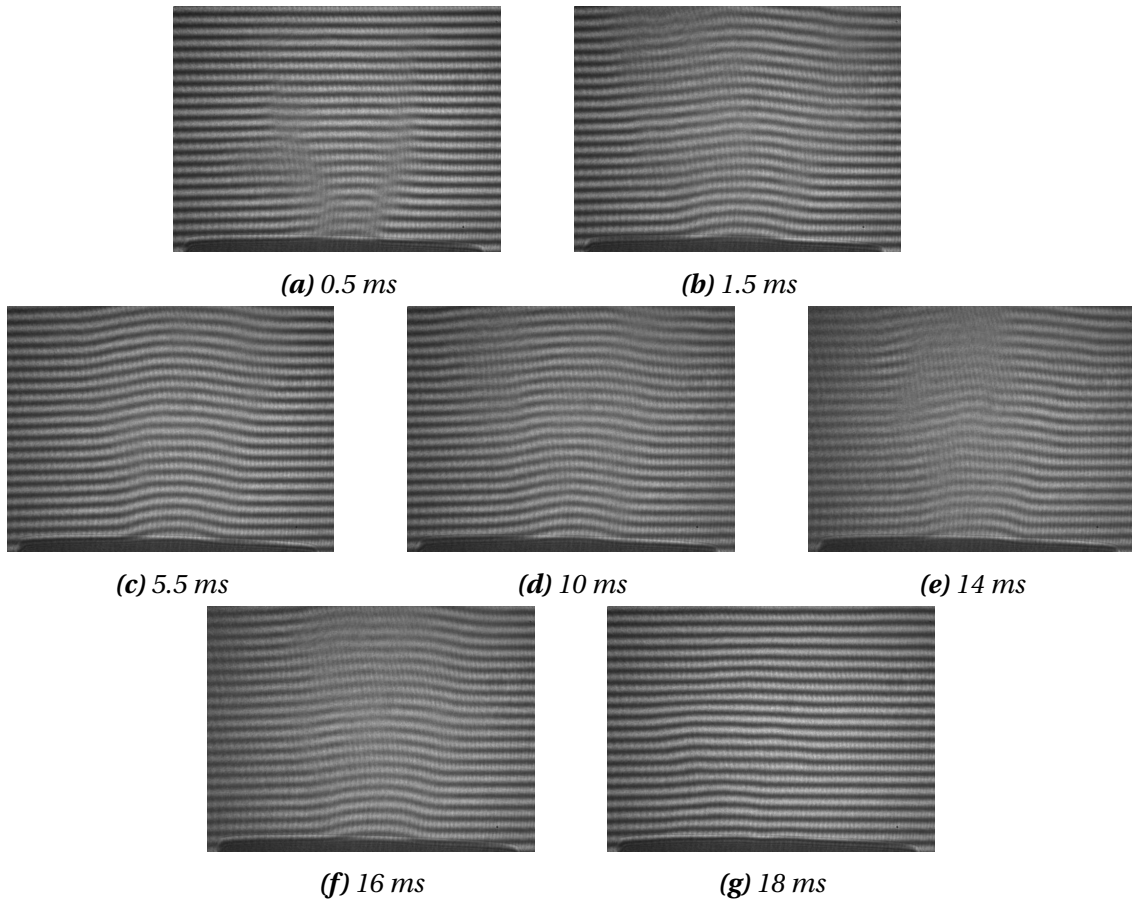


**Figure 5.2:** Images recorded at 7 bar with different exposure delay

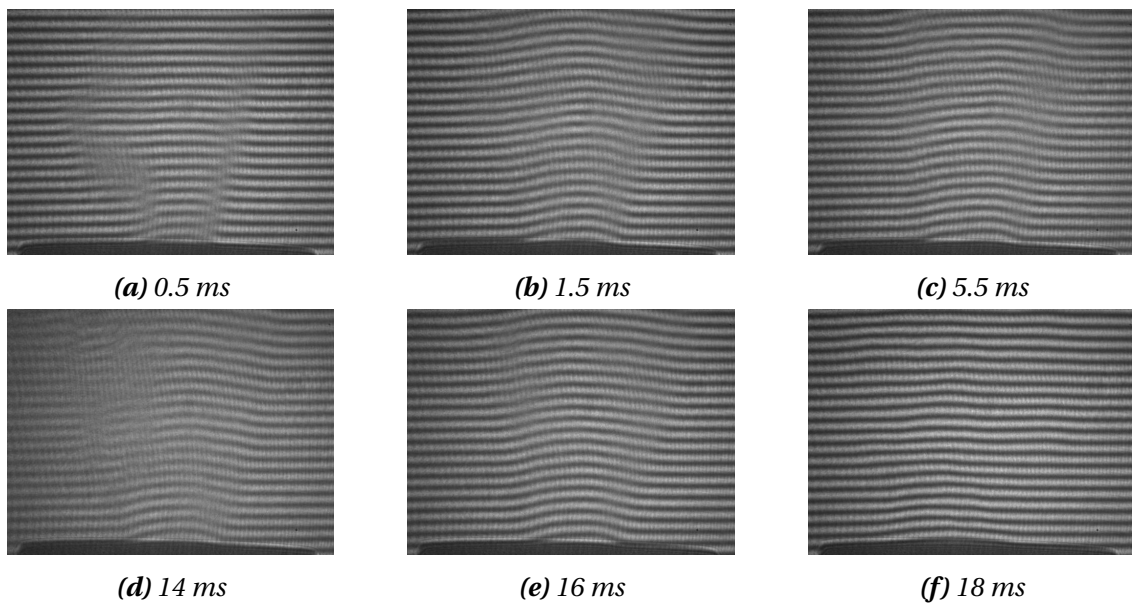


**Figure 5.3:** Images recorded at 8 bar with different exposure delay